Geostatistics applied to cross-well reflection seismic for imaging carbonate aquifers

CrossMark

Jorge Parra [a,*], Xavier Emery [b,c,1]

[a] Southwest Research Institute, USA
[b] Department of Mining Engineering, University of Chile, Chile
[c] Advanced Mining Technology Center, University of Chile, Chile

ARTICLE INFO

ABSTRACT

Cross-well seismic reflection data, acquired from a carbonate aquifer at Port Mayaca test site near the eastern boundary of Lake Okeechobee in Martin County, Florida, are used to delineate flow units in the region intercepted by two wells. The interwell impedance determined by inversion from the seismic reflection data allows us to visualize the major boundaries between the hydraulic units. The hydraulic (flow) unit properties are based on the integration of well logs and the carbonate structure, which consists of isolated vuggy carbonate units and interconnected vug systems within the carbonate matrix. The vuggy and matrix porosity logs based on Formation Micro-Imager (FMI) data provide information about highly permeable conduits at well locations. The integration of the inverted impedance and well logs using geostatistics helps us to assess the resolution of the cross-well seismic method for detecting conduits and to determine whether these conduits are continuous or discontinuous between wells. A productive water zone of the aquifer outlined by the well logs was selected for analysis and interpretation. The ELAN (Elemental Log Analysis) porosity from two wells was selected as primary data and the reflection seismic-based impedance as secondary data. The direct and cross variograms along the vertical wells capture nested structures associated with periodic carbonate units, which correspond to connected flow units between the wells. Alternatively, the horizontal variogram of impedance (secondary data) provides scale lengths that correspond to irregular boundary shapes of flow units. The ELAN porosity image obtained by cokriging exhibits three similar flow units at different depths. These units are thin conduits developed in the first well and, at about the middle of the interwell separation region, these conduits connect to thicker flow units that are intercepted by the second well. In addition, a high impedance zone (low porosity) at a depth of about 275 m, after being converted to ELAN porosity, is characterized as a more confined low porosity structure. This continuous zone corresponds to a permeability barrier in the carbonate aquifer that separates the three connected conduits observed in the cokriging image. In the zones above and below this permeability barrier, the water production is very high, which agrees with water well observations at the Port Mayaca aquifer.

1. Introduction

This study aims to integrate geophysical information to constrain the mapping of conduits in the interwell region of an aquifer test site, located about 48 km west of the Atlantic Ocean and approximately 1.6 km east of the eastern boundary of Lake Okeechobee in Martin County, south Florida. Some of the conduits are so thin that they are observed only in the Formation Micro-Imager (FMI) logs at the well locations (Parra et al., 2009). Thicker conduits are delineated by geophysical data, obtained by ground penetrating radar (GPR) and seismic techniques (Cardimona et al., 1998; Dubreuil-Boisclair et al., 2011;

McKenna and Poeter, 1995). In these studies, GPR and seismic measurements are based on cross-well transmission tomography with well separations ≤30 m. Cardimona et al. (1998) compared images of seismic reflections and GPR in a shallow aquifer. The results showed that seismic data imaged clay lenses, whereas low-frequency radar profiles did not provide clear results. In GPR measurements, depth of penetration is limited by the presence of clay minerals or high conductivity pore fluid. GPR waves can reach depths up to 30 m in low conductivity materials such as dry sand or granite. Clays, shale, and other high conductivity materials may attenuate or absorb GPR signals, greatly decreasing the depth of penetration to 1 m or less. In contrast, cross-well reflection seismic measurements can detect heterogeneities and rock physical properties with vertical and horizontal resolutions of 0.6 m and 3 m, respectively, at an interwell distance greater than 365 m (Parra et al., 2009). The goal of this study is to estimate porosity between well locations in order to identify the lateral extents of the rock

* Corresponding author at: 6220 Culebra Rd., San Antonio, TX 78023, United States. Tel.: +1 210 522 3284; fax: +1 210 522 5606.
  E-mail addresses: jparra@swri.org (J. Parra), xemery@ing.uchile.cl (X. Emery).
[1] Av. Tupper 2069 Santiago, Chile. Tel.: +56 2 29784498.

structures and their connectivity, by combining cross-well reflection seismic data and well log data.

The problem with using densely sampled secondary information (such as seismic impedance) in addition to sparsely sampled well-log measurements is a longstanding issue in subsurface mapping applications, especially in oil reservoir modeling (Abrahamsen et al., 1997; Doyen, 1988; Doyen et al., 1996; Dubrule, 1998, 2003). Bayesian approaches, such as Bayesian maximum entropy (Christakos, 1990; Christakos and Li, 1998; Wibrin et al., 2006) and Bayesian data fusion (Bogaert and Fasbender, 2008), offer a flexible solution to account for secondary information and its uncertainty, while they avoid assuming linear relationships between the variables. An alternative way of integrating secondary information without the restriction of linear models is provided by machine learning algorithms, such as artificial neuronal networks, support vector regressions, and genetic algorithms (Besaw and Rizzo, 2007; Kanevski et al., 2003; Leite and Vidal, 2011; Matsoukas et al., 1999).

In the field of geostatistics, a secondary variable that is exhaustively known in space can be used to define a trend model for the variable of interest (also called the primary variable). To this end, one can combine spatial prediction and regression techniques, leading to the so-called "kriging with a trend model", i.e., the guess field model (Chilès and Delfiner, 2012), regression kriging (Hengl et al., 2007) and external drift kriging (Goovaerts, 1997; Hudson and Wackernagel, 1994). The underlying trend model is that the primary variable has been generated by a spatial random field Z_1 such that, at each location $\mathbf{x}$, one has:

$$E\{Z_1(\mathbf{x})\} = a + bZ_2(\mathbf{x}), \tag{1}$$

where a and b are numerical coefficients, Z_2 denotes the secondary variable, and $E\{.\}$ stands for the mathematical expectation. The differences between the aforementioned approaches lie in how the regression model is calibrated and whether or not the regression coefficients (a and b) are known. From Eq. (1), it is seen that the dependence between the primary (Z_1) and secondary (Z_2) variables is essentially a functional dependence and that the secondary variable is considered as a deterministic field.

An alternative to kriging with a trend model is cokriging, which allows one to predict a variable of interest at a given location from data on this variable as well as on one or several covariates (Goovaerts, 1997; Wackernagel, 2003; Wackernagel et al., 2002). Here, all the variables are viewed as outcomes of spatial random fields, commonly with the assumption that their expected values are constant in space or, at least, constant at a local scale. In such a case, the relationship between the primary and secondary variables is reduced to a stochastic dependence, controlled by cross-correlation between the random fields. Cokriging variants include simple cokriging, in which the mean values of the random fields are assumed known, and ordinary cokriging, in which the mean values are unknown. The former implies little flexibility, as no uncertainty in the means can be taken into account (a reason global means are usually considered), while the latter often gives little importance to the secondary variable, as the weights assigned to secondary data sum to zero (Goovaerts, 1997). Several studies have compared

the performance of kriging with a trend predictors and cokriging predictors (Asli and Marcotte, 1995; Goovaerts, 2000; Juang and Lee, 1998; Pardo-Igúzquiza, 1998), but no clear conclusion can be drawn as to which is better. The main characteristics of the predictors are listed in Table 1.

For this study, we combined the advantages of cokriging and kriging with a trend model, by considering both a functional dependence and a stochastic dependence between the primary and secondary variables. These variables are considered as outcomes of cross-correlated random fields (as in simple or ordinary cokriging), but with the following additional restriction that modifies Eq. (1):

$$E\{Z_1(\mathbf{x})\} = a + bE\{Z_2(\mathbf{x})\}, \tag{2}$$

where the coefficients a and b are assumed known, while the expected values of Z_1 and Z_2 are unknown but locally constant in space. This way, the relationships between the primary and secondary variables stem not only from the correlation (second-order moment) between the associated random fields, but also from the functional dependence between their expected values (first-order moments). This variant is suitable when the variables are linearly related, which is the case for impedance and porosity.

For completeness, the stochastic simulation approach is considered as an alternative for incorporating data from different sources. Many algorithms have been proposed, based on Gaussian or indicator transforms, simulated annealing, or Bayesian models, among others (Dafflon et al., 2009; Deutsch and Cockerham, 1994; Dubreuil-Boisclair et al., 2011; Goovaerts, 1997; Pebesma, 2004). Simulation allows one to assess spatial uncertainty through the construction of multiple outcomes that reproduce the spatial variability of the true unknown fields, but none of these outcomes is a good local predictor of the true fields. Simulation is out of the scope of this work, which aims at mapping porosity rather than constructing multiple outcomes of it.

2. Data acquisition and processing

A cross-well survey was conducted at the Port Mayaca test site, Florida. This site is located about 48 km west of the Atlantic Ocean and approximately 1.6 km east of the eastern boundary of Lake Okeechobee in Martin County, south Florida. The measurements were taken between monitoring wells MF-37 and EXPM-1 (located at east coordinates 0 and 382.6 m, respectively), using a Z-Seis piezoceramic X series source and a 10-level hydrophone system (Parra et al., 2003, 2006, 2009). Multiple source and detector measurements were taken in the depth interval from 121.9 to 518.2 m. The objectives of the survey were to map the flow unit variability in the region between the two wells, to assess whether the high-resolution seismic survey could resolve and detect zones of high water production, and to map the matrix porosity and permeability. In this study, we consider the porosity logs from wells MF-37 and EXPM-1 and the P-wave impedance data obtained by inverting the cross-well reflection seismic measurements,

Table 1
Main characteristics of kriging and cokriging predictors.

Kriging with a trend	Simple cokriging	Ordinary cokriging
Linear functional dependence between primary and secondary variables (trend model)	No functional dependence between primary and secondary variables	No functional dependence between primary and secondary variables
No stochastic dependence between primary and secondary variables	Linear stochastic dependence (correlation) between primary and secondary variables	Linear stochastic dependence (correlation) between primary and secondary variables
Secondary variable exhaustively known	Secondary variable may be partially known	Secondary variable may be partially known
Implementation in a local neighborhood when too many primary data points are available	Implementation in a local neighborhood when too many primary or secondary data points are available	Implementation in a local neighborhood when too many primary or secondary data points are available
	No uncertainty in the mean values, generally taken as constant in space	Total uncertainty in the mean values, which are constant at the neighborhood scale
Need for the variogram of the primary variable only	Need for a coregionalization model (direct and cross variograms)	Need for a coregionalization model (direct and cross variograms)

which were presented by Parra et al. (2009). The processing method used for inversion was a band-limited inversion algorithm described by Olderburg et al. (1983) and Parra et al. (2006). We selected the P-wave impedance rather than P-wave velocity, because the impedance image captures the variability of lateral structures in the limestone formation. The advantages of using reflections for cross-well imaging applications, as opposed to conventional direct arrival travel-time tomography, are: 1) imaging ability at and below the bottoms of the wells, where the reservoir is sometime located; 2) improved vertical resolution over tomography; and 3) reduction of fundamental tomography imaging artifacts caused by aperture limitations and anisotropy (Beydoun et al., 1988; Khalil et al., 1993; Lazaratos, 1993).

From the seismic impedance section obtained by the inversion of reflection data, we selected a high water production zone below the top confining unit of the aquifer, at a depth of between 250 m and 332 m, with a resolution of 3 m in the east–west direction and 0.6 m in depth (Fig. 1). The impedance image captures lateral heterogeneities in the interwell region that are not observed in the velocity tomogram given in Parra et al. (2009) and that will be used as secondary data to delineate the heterogeneities of the aquifer, where high water production has been observed (Bennett and Recrenwald, 2002).

In addition, the Elemental Log Analysis (ELAN, Schlumberger propriety software) porosity (Fig. 2), vuggy porosity, matrix porosity, total porosity, and impedance logs were integrated with Formation Micro Image (FMI) data at the well locations, with a resolution of 0.15 m along the wells, to identify conduits that could be delineated with cross-well reflection seismic (Parra et al., 2009). ELAN depends on three porosity tools – density, neutron, and sonic – to calculate total porosity.

3. Geostatistical modeling of porosity and impedance data

To cross-correlate porosity (primary variable) with P-wave impedance (secondary variable), the latter variable was interpolated at the two wells by assigning to each well location the value of the closest P-wave impedance data. The analysis of correlation coefficients and scatter plots indicates that there is a moderate but significant dependence between P-wave impedance and ELAN porosity, with a correlation coefficient of -0.43, but no relevant dependence between P-wave impedance and other types of porosity (matrix, vuggy, and total porosity).

Hereafter we focus on the problem of predicting ELAN porosity in the interwell region, using P-wave impedance as a covariate. In Sections 3.1 and 3.2, these variables are viewed as outcomes of spatial random fields and are characterized by their first- and second-order moments (mean values and variograms). For inference purposes, we assume that these moments are invariant under a spatial translation, at least at a small scale (assumption of local stationary) (Chilès and Delfiner, 2012).
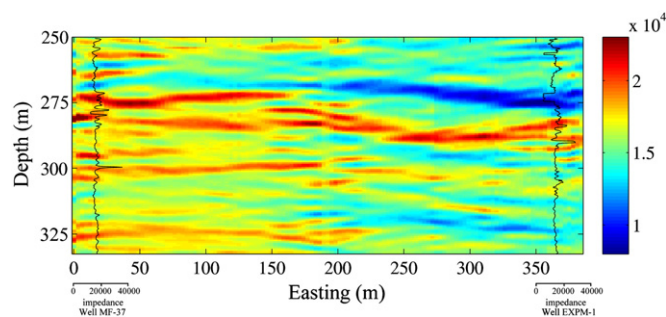

Fig. 1. P-wave impedance (g/cm³) (ft/s) used as secondary data for variogram analysis and cokriging. Well log impedances computed from density and velocity logs from wells MF-37 and EXPM-1 are superimposed to provide better visual comparison to the P-wave impedance.

3.1. Modeling the relationship between mean values

The mean values of the variables for the well data are indicated in Table 2. Accordingly, there is an inverse relationship between the mean values of ELAN porosity and of P-wave impedance. This relationship can be modeled in the following way:

$$\text{mean porosity} + 1.402 \times 10^{-5}\text{mean impedance} = 0.615. \quad (3)$$

The model given by Eq. (2) is corroborated by plotting the porosity data as a function of the impedance data (Fig. 3) and checking that the experimental points fluctuate around the model given by Eq. (3). This can be done by considering the P-wave impedance data (Fig. 3A), as well as the impedance data logged at wells EXPM-1 and MF-37 (Fig. 3B), insofar as both types of impedance (P-wave impedance and logged impedance) are expected to have the same mean value.

3.2. Modeling the spatial correlation structure

The P-wave impedance map (Fig. 1) shows a strong anisotropy, with much greater spatial continuity along the east–west direction than along the vertical direction (direction of the wells). To model the spatial continuity, variograms are calculated along these two directions. Because two variables (ELAN porosity as the primary variable and P-wave impedance as the secondary variable) are under consideration, three variograms can be defined:

(1) Direct variogram of ELAN porosity

We define the ELAN porosity as Z_1 (viewed as a spatial random field) and the spatial location as $\mathbf{x}$. The direct variogram of ELAN porosity for a lag separation vector $\mathbf{h}$ is defined as:

$$\gamma_1(\mathbf{h}) = \frac{1}{2}E\left\{[Z_1(\mathbf{x}+\mathbf{h})-Z_1(\mathbf{x})]^2\right\}. \quad (4)$$

Experimentally, this variogram is estimated by calculating the mean squared difference between porosity data at locations separated by $\mathbf{h}$ (Chilès and Delfiner, 2012; Goovaerts, 1997). It is quite easy to calculate the experimental variogram along the vertical direction (well direction) for lag distances that are a multiple of 0.15 m (Fig. 4A). In the east–west direction, the calculation is limited to a single lag distance of 382.6 m, which corresponds to the distance that separates the two wells (Fig. 4B).

(2) Direct variogram of P-wave impedance

The direct variogram of P-wave impedance (denoted by Z_2) for a lag separation vector $\mathbf{h}$ is defined as:

$$\gamma_2(\mathbf{h}) = \frac{1}{2}E\left\{[Z_2(\mathbf{x}+\mathbf{h})-Z_2(\mathbf{x})]^2\right\}. \quad (5)$$

This variogram can be estimated along the vertical direction for lag distances that are a multiple of 0.6 m (Fig. 4C) and along the east–west direction for lag distances that are a multiple of 3 m (Fig. 4D). These distances correspond to the grid mesh at which the P-wave impedance is available.

(3) Cross variogram between ELAN porosity and P-wave impedance

This variogram allows us to model the joint correlation structure of ELAN porosity and P-wave impedance. It is defined as:

$$\gamma_{12}(\mathbf{h}) = \frac{1}{2}E\{[Z_1(\mathbf{x}+\mathbf{h})-Z_1(\mathbf{x})][Z_2(\mathbf{x}+\mathbf{h})-Z_2(\mathbf{x})]\}. \quad (6)$$

To calculate the experimental variogram, we consider porosity data at the well locations along with P-wave impedance data at the same locations. The calculations are performed for lag distances that
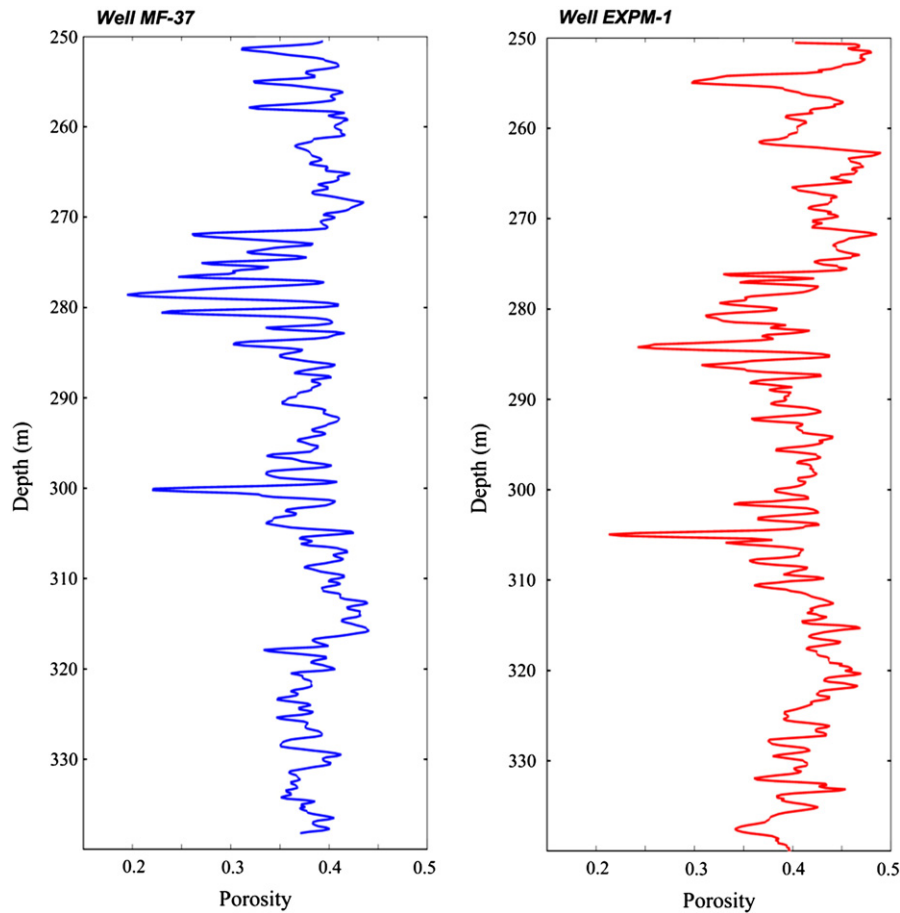
Fig. 2. ELAN porosity well logs between depths of 250 m and 332 m, used as primary data for variogram analysis and cokriging.

are a multiple of 0.6 m along the vertical direction (Fig. 4E) and for a single distance of 382.6 m along the east–west direction (Fig. 4F). It should be noted that the cross variogram has negative values, which is consistent with the negative correlation observed between the two variables: if ELAN porosity at location $\mathbf{x}+\mathbf{h}$ is greater than at location $\mathbf{x}$, then the reverse should happen for P-wave impedance, which implies a negative value for the cross variogram (Eq. (6)).

Several interesting features can be seen in the experimental variograms. First, the shapes of the direct and cross variograms along the vertical direction are similar, with a dampened periodic behavior. Second, the variogram of P-wave impedance along the east–west direction increases at large distances, which may reflect a large range structure or a trend between the two wells. The other two variograms are mostly unknown in this direction but, based on what is observed for the vertical direction, one can assume that their shapes are similar to that of the direct variogram of P-wave impedance.

The experimental variograms are fitted by using combinations of the following five basic nested structures (Chilès and Delfiner, 2012):

- A nugget effect (NUG).
- Two anisotropic short- to medium-range spherical models — one (SPH1) with ranges of 60 m (east–west direction) and 1.5 m (vertical direction), and the other (SPH2) with ranges of 90 m (east–west direction) and 3 m (vertical direction).
- One anisotropic dampened periodic model (BESSEL-J), with a scale factor of 3.7 m (corresponding to a half-period of about 14 m) along the vertical direction (to account for periodicity) and infinite along the east–west direction (no observed periodicity).
- One anisotropic large-range cubic model (CUB), with a range of 750 m along the east–west direction (to account for the large-scale structure or trend) and infinite along the vertical direction (no observed trend).

The above ranges and scale factors were chosen by trial and error to fit the slope changes of the experimental variograms at short and medium distances (case of the SPH models), the period along the vertical direction (case of the BESSEL-J model), and the slope and behavior at large distances along the east–west direction (case of the CUB model). To complete the specification of each model, we determined the contribution of each basic structure to each variogram using an iterative procedure (Emery, 2010) that provided the models that minimize the squared deviations between experimental and fitted variograms. The final model is:

$$\gamma_{11}(\mathbf{h}) = 0.059 \times 10^{-4} NUG + 12.0 \times 10^{-4} SPH1 + 6.11 \times 10^{-8} SPH2 \\ + 6.47 \times 10^{-4} BESSELJ + 11.0 \times 10^{-4} CUB$$

$$\gamma_{12}(\mathbf{h}) = -0.012 NUG - 0.232 SPH1 - 0.372 SPH2 \\ -29.0 BESSELJ - 86.8 CUB$$

$$\gamma_{22}(\mathbf{h}) = 24.90 NUG + 46.50 SPH1 + 2.28 \times 10^6 SPH2 \\ + 1.85 \times 10^6 BESSELJ + 7.00 \times 10^6 CUB.$$

$$(7)$$

As shown in Fig. 4, the periodic behavior along the vertical direction is well reproduced. Compared to the direct variograms, the cross

Table 2
Mean values of ELAN porosity and P-wave impedance.

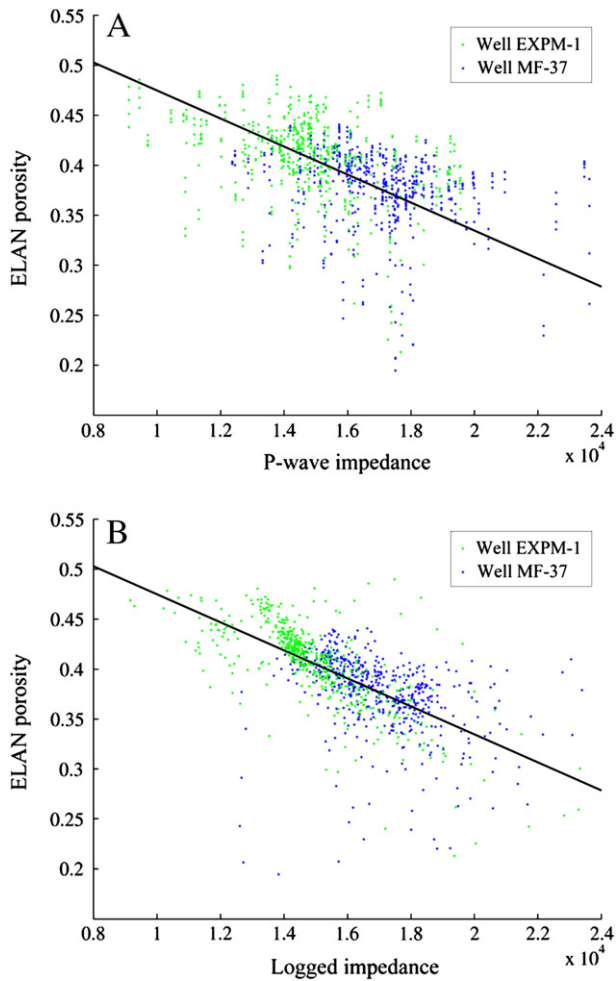|	ELAN porosity	P-wave impedance
Well MF-37	0.3760	17,074.2
Well EXPM-1	0.4082	14,777.1
Average	0.3921	15,925.6

Fig. 3. Scatter plots of ELAN porosity (ordinate) versus A) P-wave impedance, and B) logged impedance, computed from density and velocity logs.

variogram has a smoother behavior near the origin, which is explained because the less regular structures (NUG, SPH1, and SPH2) have a small contribution (Eq. (7)). The fitting along the east–west direction mainly relies on the variogram of P-wave impedance and on a single point (at a distance of 382.6 m) for the variogram of ELAN porosity and for the cross variogram.

4. Spatial prediction of porosity

Having specified the spatial dependence between ELAN porosity and P-wave impedance, it is now possible to predict the porosity in the interwell region via cokriging. A particular type of cokriging is used in which the mean values of porosity and impedance are assumed unknown, but related through Eq. (3) (Emery, 2012). This allows the mean values to vary spatially at a large scale, although they are considered as locally constant, and also creates a functional dependence relationship between the two variables.

The input parameters for cokriging are the primary and secondary data (ELAN porosity at the well locations and P-wave impedance in the interwell region), the relationship between the mean values of porosity and impedance (Eq. (3)), the modeled direct and cross variograms (Eq. (7)), and the 'local neighborhood.' The local neighborhood was designed to include up to 49 data points of the interwell region (P-wave impedance data contained in a moving window of size 25 m×5 m centered at the location of interest) and up to 48 well data points (porosity data at well logs with a depth difference of no more than 2.5 m from the depth of the location of interest).

The prediction was performed at the nodes of the grid on which the P-wave impedance is known (interwell section). The predicted porosity is displayed in Fig. 5A. The prediction globally exhibits the same structure as the P-wave impedance (Fig. 1), with a negative correlation.

For comparison, two other ways to predict porosity were tested:

- Traditional ordinary cokriging (Fig. 5B), which is similar to the proposed cokriging approach, except that it accounts only for the variogram model and ignores the relationship between the mean values of porosity and impedance (Eq. (3));
- Regression kriging (Fig. 5C), which consists of fitting a linear regression of the primary data (porosity) upon the secondary data (impedance), deriving the residuals of the regression at each well location, and kriging these residuals at the target grid nodes. As the variogram of the residuals can only be calculated along the vertical drill hole direction, an isotropic variogram model is considered for kriging (namely, an exponential model with a practical range of 2 m), and the anisotropic features of porosity are assumed to be taken into account through the regression model (Eq. (1)).

On one hand, ordinary cokriging provides a map with many fewer details than the other two methods. This can be explained because a property of ordinary cokriging is to assign weights to the secondary data that sum to zero. This implies that the secondary variable (P-wave impedance) makes a small contribution to the prediction in comparison to the primary variable (ELAN porosity) (Goovaerts, 1997). This is the cost incurred by taking into account only the stochastic dependence relationship between the primary and secondary variables, which is not strong (the correlation coefficient is −0.43), and ignoring the functional dependence relationship between these variables.

On the other hand, regression kriging leads to a more contrasted map, which is almost a linear transformation of the impedance map (Fig. 1). This is because the residual has a short range variogram of 2 m, so that its prediction in the interwell region by simple kriging is practically equal to its mean value, i.e., 0. Apart from variogram analysis (assumption of isotropy for the residual variogram), an inconvenient aspect of this approach is that the prediction of porosity at a given location depends only on the collocated impedance data, thus it is sensitive to any inaccuracy in this data. For instance, the local artifact (vertical band) in the impedance map near the east coordinate (190 m) also appears in the porosity map (Fig. 5C). Ideally, the impedance variable should vary smoothly in space, with no abrupt fluctuation, to be considered an accurate measure of the trend in the porosity (Eq. (1)).

The proposed approach (cokriging with linearly related means, Fig. 5A) provides a more detailed and contrasted map than ordinary cokriging and regression kriging. Furthermore, unlike regression kriging, the local artifact in the impedance map (vertical band around the east location at 190 m) is hardly perceptible in the porosity map. This is because the predicted porosity at a given location no longer depends on collocated impedance data, but on a weighted average of the impedance data situated around the target location (one could even consider the case of missing impedance data, for which a porosity prediction could still be obtained). The weighting rests on the joint spatial correlation structure of the primary and secondary variables, hence the importance of considering a stochastic dependence between these variables in addition to a functional dependence.

5. Discussion

The experimental variograms provide information on the structure of the aquifer. The variograms along the vertical direction for the primary and secondary data have similar shapes. Although the nugget effect may reflect well data measurement errors and does not contribute to the final porosity image, the structures with ranges
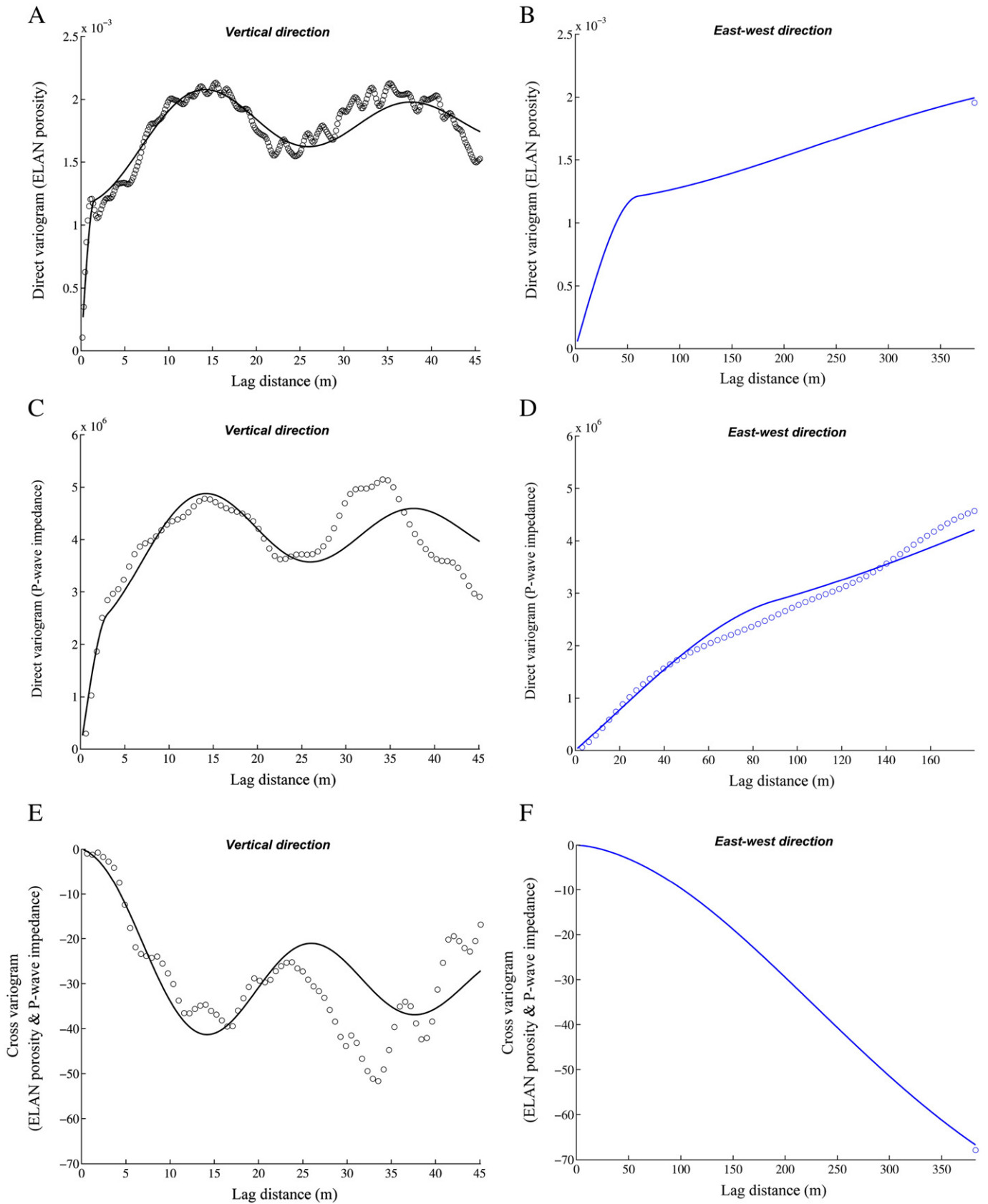
Fig. 4. Experimental (circles) and modeled (solid lines) variograms for ELAN porosity and P-wave impedance, along vertical and east–west directions.

of 1.5 and 3 m are delineated by the ELAN porosity image (Fig. 5A). These correspond to interconnected conduits embedded in layered structures, which are formed by low and high impedance zones (Fig. 1). These impedance zones are obtained by the inversion of re-flection data that provide the layered boundaries between the carbon-ate rock formations.

A

Cokriging with linked means

B

Ordinary cokriging
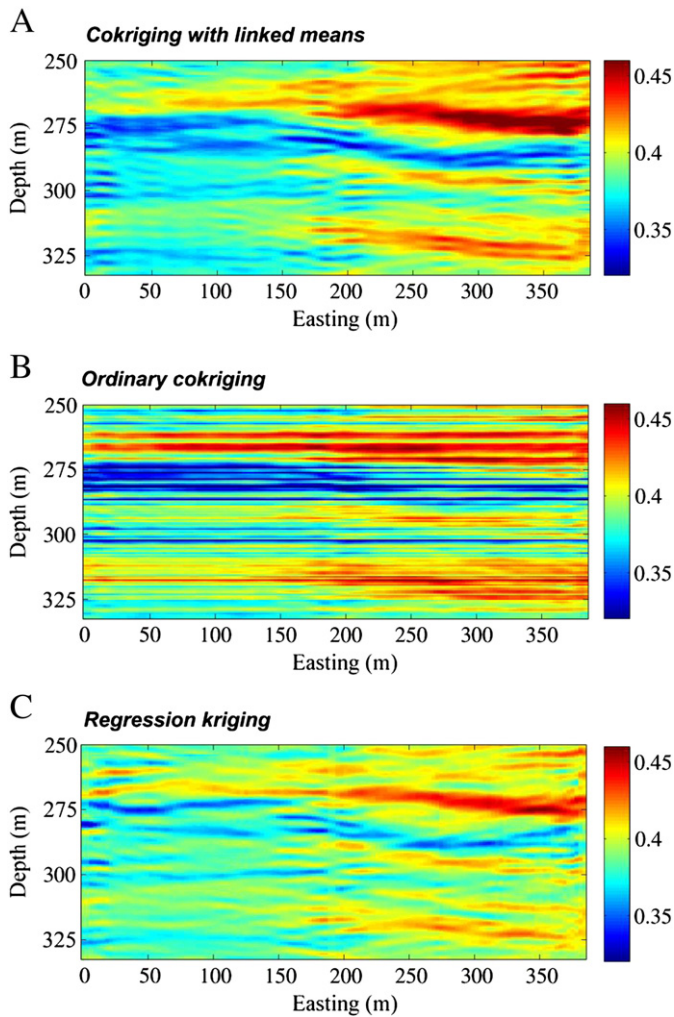

C

Regression kriging

Fig. 5. Comparison of ELAN porosity images obtained by cokriging with (A) linearly related means, (B) ordinary cokriging, and (C) regression kriging.

The impedance contrasts between these flow units are observed as pseudo periodic shapes in the vertical variograms of the primary and secondary data and the cross variogram as well, with a period of between 21 and 27 m. This variogram characteristic relates to permeable carbonate units that are associated with interconnected matrix porosity having an average porosity greater than 40% and can be better visualized in the cokriging image (Fig. 5A) with the help of well logs.

In particular, two thin conduits are observed near well MF-37 (east coordinate 0 m) at 265 m and 270 m depth. Both conduits laterally increase in porosity up to about 150 m to the east, where they connect to a thicker flow unit of higher porosity that is intercepted by well EXPM-1 (east coordinate 382.6 m). A second conduit observed at a depth of 295 m near well MF-37 forms a flow unit that increases laterally in porosity toward a higher porosity flow unit that is also intercepted by well EXPM-1. The last conduits near well MF-37 are observed at a depth of about 320 m and have structural characteristics similar to those of the upper flow unit. The connectivity of these three flow units can also be visualized in the ordinary cokriging image (Fig. 5B), but without the lateral variable thicknesses that are captured by the proposed cokriging approach.

In addition, Fig. 5A shows a continuous low porosity structure between both wells in the depth interval of 275–290 m. The presence of this low porosity zone connected between both wells is sustained by low porosity signature characteristics observed in both well logs.

Within this structure there is a carbonate unit 7–8 m thick that is not connected between the matrix and the vuggy carbonate that separates the upper and lower water production zones. As a result, the low porosity structure in the depth interval of 275–290 m is considered a permeability barrier in the aquifer by Bennett and Recrenwald (2002).

The east–west direction variograms show intermediate (60–90 m) and large (>300 m) ranges that characterize lateral and uniform structures above and below the low porosity structure. These lateral structures are observed approximately every 60 m in the cokriged porosity image, which outlines the major irregular boundary shapes of the flow units. In addition, the zone of 260–275 m depth clearly shows the porosity connectivity from well MF-37 to well EXPM-1. At well MF-37, conduits about 3 m thick are developed to form a heterogeneous structure that, at 180 m from well MF-37, merges into a thicker and more porous/continuous flow unit, which is intercepted by well EXPM-1. These structural features are not outlined by the P-wave impedance image but are clearly identified in the cokriged porosity image. This image is consistent with the flow unit connectivity that is supported by the high water production and hydrology conditions of the aquifer. These conditions are also observed in the depth interval at 305–320 m, where the structure pattern is similar to that of the depth interval at 250–290 m. The porosity image outlines the major carbonate units well, but thin conduits of 0.15–0.3 m are not delineated by cokriging due to the limited resolution of the cross-well reflection seismic data. For example, a thin conduit of 0.1 m observed in FMI logs (Parra et al., 2009) at a depth of 283.5 m in well MF-37 that carries water to well EXPM-1 is not captured by the cokriging image. This conduit, which is in a zone of high impedance in the horizontal direction interval of 0–180 m (low porosity), merges into a higher porosity interval intercepted by well EXPM-1 at a depth of 290 m. We expect that this conduit is associated with secondary porosity (vugs) developed in a brittle limestone.

6. Conclusions

Cross-well seismic reflection data provide information on the intrinsic properties of the formation and, with well log data (Parra et al., 2009), resolve conduits (interconnected vuggy porosity) seen in the porosity well logs. The ELAN porosity image clearly shows the variation of the flow units in the interwell region. This was achieved by a complete variogram analysis and cokriging. The vertical variograms of the primary and secondary data, as well as the cross variogram, show the presence of a nested structure that is associated with periodic flow units in the aquifer. The east–west direction variograms show intermediate and large range structures that characterize lateral and uniform structures above and below the low porosity zone at a depth of about 275 m. These lateral structures are observed approximately every 60 m in the ELAN porosity image in the horizontal east–west direction, which outlines the major irregular boundary shapes of the flow units. These units are observed at depths of 265 m, 295 m and 320 m in the cokriging image and are formed by thin conduits intercepted by well MF-37 that merge into thicker and more porous structures intercepted by well EXPM-1.

The cokriging method provides a good description of highly interconnected vuggy porosity that is associated with high water production. The high impedance zone at about 275 m, after being transformed to porosity, is more uniform; it is shown as a continuous, lower porosity structure that is considered a permeability barrier in carbonate aquifers. In zones above and below the permeability barrier, water production is very high, which agrees with water well observations (Bennett and Recrenwald, 2002). Although the porosity image outlines the major flow units, thin conduits of 0.15–0.3 m are not captured by cokriging because of the limited resolution of the current cross-well reflection seismic technique.

Acknowledgments

References

Abrahamsen, P., Hektoen, A.L., Holden, L., Munthe, K.L., 1997. Seismic impedance and porosity: support effects. In: Baafi, E.Y., Schofield, N. (Eds.), Geostatistics Wollongong '96. Kluwer, Dordrecht, pp. 489–500.

Asli, M., Marcotte, D., 1995. Comparison of approaches to spatial estimation in a bivariate context. Mathematical Geology 27 (5), 641–658.

Bennett, M.W., Recrenwald, E.E., 2002. Hydrogeologic investigation of the Floridian Aquifer System, Port Mayaca Site, Martin County, Florida: Preliminary Report, SFWMED, West Palm Beach.

Besaw, L.E., Rizzo, D.M., 2007. Stochastic simulation and spatial estimation with multiple data types using artificial neural networks. Water Resources Research 43, W11409.

Beydoun, W.B., Delvaux, J., Mendes, M., Noual, G., Tarantola, A., 1988. Practical aspects of an elastic migration/inversion of crosshole data for reservoir characterization: a Paris Basin example. Geophysics 54, 1587–1595.

Bogaert, Fasbender, 2008. Bayesian data fusion applied to water table spatial mapping. Water Resources Research 44 (12), W12422.

Cardimona, S.J., Clement, W.P., Kadinsky-Cade, K., 1998. Seismic reflection and ground penetrating radar imaging of a shallow aquifer. Geophysics 63, 1310–1317.

Chilès, J.P., Delfiner, P., 2012. Geostatistics: Modeling Spatial Uncertainty. Wiley, New York (699 pp.).

Christakos, G., 1990. A Bayesian/maximum-entropy view to the spatial estimation problem. Mathematical Geology 22 (7), 763–777.

Christakos, G., Li, X.Y., 1998. Bayesian maximum entropy analysis and mapping: a farewell to kriging estimators? Mathematical Geology 30 (4), 435–462.

Dafflon, B., Irving, J., Holliger, K., 2009. Use of high-resolution geophysical data to characterize heterogeneous aquifers: influence of data integration method on hydrological predictions. Water Resources Research 45, W09407.

Deutsch, C.V., Cockerham, P.V., 1994. Geostatistical modeling of permeability with annealing cosimulation (ACS). SPE 69th Annual Technical Conference and Exhibition, New Orleans: SPE, 28413.

Doyen, P.M., 1988. Porosity from seismic data: a geostatistical approach. Geophysics 53 (10), 1263–1276.

Doyen, P.M., den Boer, L.D., Pillet, W.R., 1996. Seismic porosity mapping in the Ekofisk field using a new form of collocated cokriging. SPE 71st Annual Technical Conference and Exhibition, Denver: SPE, 36498.

Dubreuil-Boisclair, C., Gloaguen, E., Marcotte, D., Giroux, B., 2011. Heterogeneous aquifer characterization from ground-penetrating radar tomography and borehole hydrogeophysical data using nonlinear Bayesian simulations. Geophysics 76 (4), 1–13.

Dubrule, O., 1998. Geostatistics in Petroleum Geology. American Association of Petroleum Geologists, Tulsa.

Dubrule, O., 2003. Geostatistics for Seismic Data Integration in Earth Models. Society of Exploration Geophysicists (279 pp.).

Emery, X., 2010. Iterative algorithms for fitting a linear model of coregionalization. Computers & Geosciences 36 (9), 1150–1160.

Emery, X., 2012. Cokriging random fields with means related by known linear combinations. Computers & Geosciences 38 (1), 136–144.

Goovaerts, P., 1997. Geostatistics for Natural Resources Evaluation. Oxford University Press, New York (480 pp.).

Goovaerts, P., 2000. Geostatistical approaches for incorporating elevation into the spatial interpolation of rainfall. Journal of Hydrology 228 (1–2), 113–129.

Hengl, T., Heuvelink, G.B.M., Rossiter, D.G., 2007. About regression-kriging: from equation to case study. Computers & Geosciences 33, 1301–1315.

Hudson, G., Wackernagel, H., 1994. Mapping temperature using kriging with external drift — theory and an example from Scotland. International Journal of Climatology 14 (1), 77–91.

Juang, K.W., Lee, D.Y., 1998. A comparison of three kriging methods using auxiliary variables in heavy-metal contaminated soils. Journal of Environmental Quality 27 (2), 355–363.

Kanevski, M., Demyanov, V., Pozdnukhov, A., Parkin, R., Savelieva, E., Timonin, V., Maignan, M., 2003. Advanced geostatistical and machine-learning models for spatial data analysis of radioactively contaminated regions. Environmental Science and Pollution Research, Special Issue 137–149.

Khalil, A.A., Stewart, R.R., Henley, D.C., 1993. Full-waveform processing and interpretation of kilohertz cross-well seismic data. Geophysics 58, 1248–1257.

Lazaratos, S.K., 1993. Cross-well reflection imaging. Ph.D. Thesis: Stanford University.

Leite, E.P., Vidal, A.C., 2011. 3D porosity prediction from seismic inversion and neural networks. Computers & Geosciences 37 (8), 1174–1180.

Matsoukas, C., Islam, S., Kothari, R., 1999. Fusion of radar and rain gage measurements for an accurate estimation of rainfall. Journal of Geophysical Research-Atmospheres 104 (D24), 31437–31450.

McKenna, S.A., Poeter, E.P., 1995. Field example of data fusion in site characterization. Water Resources Research 31, 3229–3240.

Olderburg, D.W., Scheuer, T., Levy, S., 1983. Recovery of the acoustic impedance from reflection seismograms. Geophysics 48, 1318–1337.

Pardo-Igúzquiza, E., 1998. Comparison of geostatistical methods for estimating the areal average climatological rainfall mean using data on precipitation and topography. International Journal of Climatology 18 (9), 1031–1047.

Parra, J.O., Hackert, C.L., Bennett, M., Collier, H.A., 2003. Permeability and porosity images based on NMR, sonic, and seismic reflectivity: application to a carbonate aquifer. The Leading Edge 22, 1102–1108.

Parra, J.O., Hackert, C.L., Bennett, W.M., 2006. Permeability and porosity images based on P-wave surface seismic data: application to a South Florida aquifer. Water Resources Research 42 (2), W02415.

Parra, J.O., Hackert, C.L., Richardson, E., Clayton, N., 2009. Porosity and permeability images based on crosswell seismic measurements integrated with FMI logs at the Port Mayaca aquifer, South Florida. The Leading Edge 28, 1212–1219.

Pebesma, E.J., 2004. Multivariable geostatistics in S: the Gstat package. Computers & Geosciences 30 (7), 683–691.

Wackernagel, H., 2003. Multivariate Geostatistics: An Introduction with Applications, 3rd ed. Springer, Berlin (387 pp.).

Wackernagel, H., Bertino, L., Sierra, J.P., González del Río, J., 2002. Multivariate kriging for interpolating with data from different sources. In: Anderson, C.W., Barnett, V., Chatwin, P., El Shaarawi, A.H. (Eds.), Quantitative Methods for Current Environmental Issues. Springer-Verlag, London, pp. 57–75.

Wibrin, M.A., Bogaert, P., Fasbender, D., 2006. Combining categorical and continuous spatial information within the Bayesian maximum entropy paradigm. Stochastic Environmental Research and Risk Assessment 20, 381–467.